星震学 (Asteroseismology)

1. 星震学とは

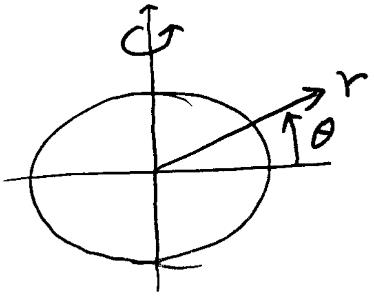

星の内部構造の診断
(進化)

$$\left.\begin{array}{l} T(r,\theta) \\ \rho(r,\theta) \\ \Omega(r,\theta) \\ B(r,\theta) \end{array}\right\} \text{未知物理量}$$

M (total mass)

診断手段

波動の観測

音波
重力波
表面波

慣性波
ロスビー波
アルフベン波
⋮

周期
振幅

順問題 (Forward Problem)

Standard Model との比較　　　太陽

(パラメータ操作)　　　星.

⇕

物理的基礎概念

逆問題 (Inverse Problem)

太陽.

星.

$T(r)$

$\rho(r)$

$\Omega(r)$

積分方程式.

太陽 : 2次元　　　(k, ω) 図

星 : 点.　　　ω 図

Asymptotic analysis

$$\frac{d^2\phi}{dr^2} + (\omega^2 - V(r))\phi = 0$$ （波動方程式）

$$\Phi_{n\ell m} = \Phi_{n\ell}(r)\, Y_\ell^m(\theta,\varphi)$$

$\ell \ll n$

$$\nu_{n\ell} = \nu_0 - \ell(\ell+1)D_0 + [\Delta\nu_0 + \ell(\ell+1)d_0]\underbrace{\left(n+\frac{\ell}{2}-n_0\right)}_{\overset{\shortparallel}{\varepsilon}}$$

$$\Delta\nu_0 = \left[2\int_0^R \frac{dr}{c}\right]^{-1}$$

$$D_0 = \frac{1}{4\pi^2(n_0+\varepsilon)}\left[\frac{c(R)}{R} - \int_0^R \frac{dc}{dr}\frac{dr}{r}\right]$$

$$\nu_{n+1,\ell} - \nu_{n,\ell} = \Delta\nu_0$$

$$\nu_{n,\ell} - \nu_{n-1,\ell+2} \simeq 2(2\ell+3)D_0$$

Rotatinal Splitting

$$\omega = \omega_0 - m(1-C)\Omega + o(\Omega^2)$$

$$C = \int_0^R \rho r^2[2\xi_r\xi_\ell + \xi_\ell^2]\,dr \Big/ \int_0^R \rho r^2[\xi_r^2 + \ell(\ell+1)\xi_\ell^2]\,dr$$

2. 観測方法

2.1 光度変化

太陽 : $\Delta I/I$ 1×10^{-6} $(\ell \lesssim$

地球大気のゆらぎによる limit が大きい

2.2 視線速度変化

太陽 $15\,\mathrm{cm/s}$

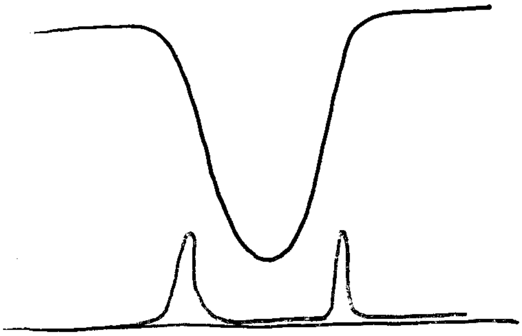

continuum と absorption の相対比.

（ゆらぎの影響小さい）

3. 星震学の現状

3.1 晩期型星 (late type Stars) (太陽型)

α CMi (プロキオン), α Cen , ε Eri, α Boo,

Forward problem. ⇒ ages, masses, mixing

ε Eri : old or young ?

(radial Velocity

3.2 Ap Stars

(photometry)

$\Delta I \sim 1 \sim 100$ m mag.

oblique rot. model

3.3 White Dwarf (白色矮星)

PNNV	DOV	DBV	DAV
?	?	HeI	H
(C, O)			

Period change $\Longrightarrow$ structure ch.
(Cooling time)

continuous obs. $\Longrightarrow$ multi-modes

3.4 早期型星

Be星（高速自転星）

line profile variation

$\boxed{\ell \lesssim 10}$

"Doppler Imaging"

4. 将来の展望

8m 望遠鏡の時代

星でも

"逆問題 "

に取組めるようになる。

スペース の有利性

コストの問題

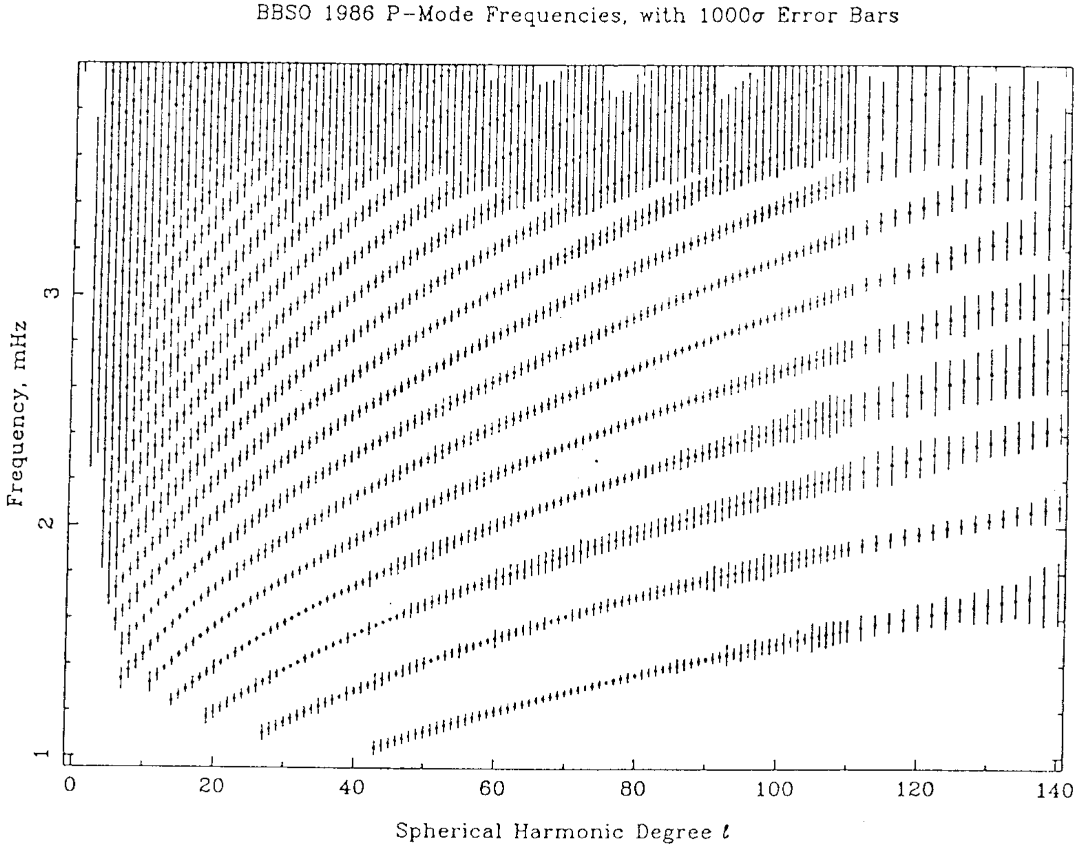

Fig. 1. Plot showing the observed 1986 p-mode frequencies from BBSO, along with error bars which have been magnified 1000 times. Modes with periods up to 16 minutes are seen, and the 1σ frequency uncertainties are as low as 10 nHz for some modes. The lowest frequency ridge shown has $n = 1$.

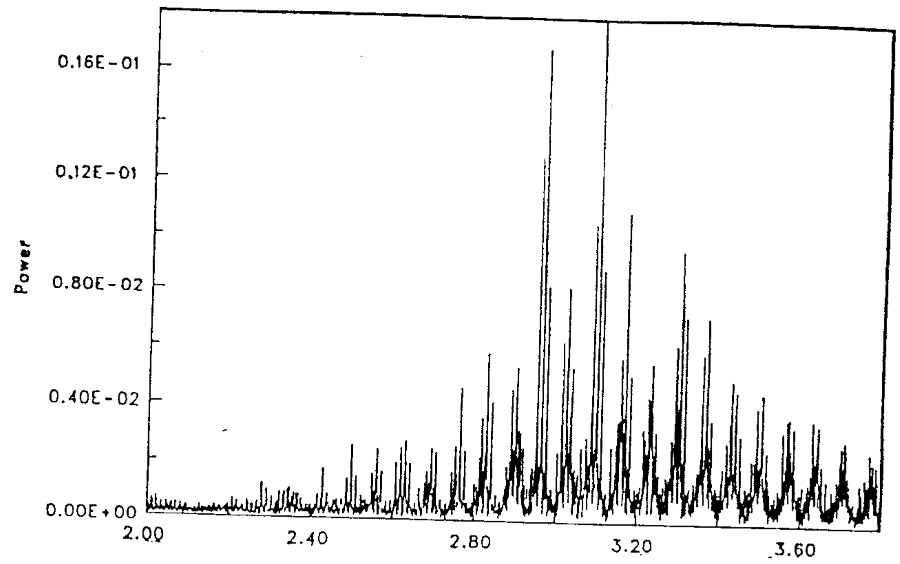

Fig. 3a. 67 days single channel power spectrum.

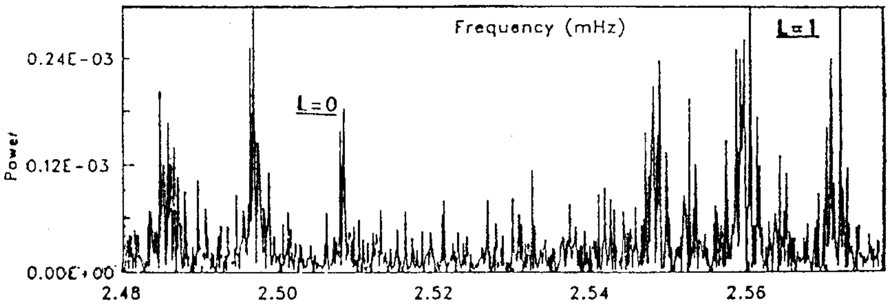

Fig. 3b. Expanded portion of the power spectrum.

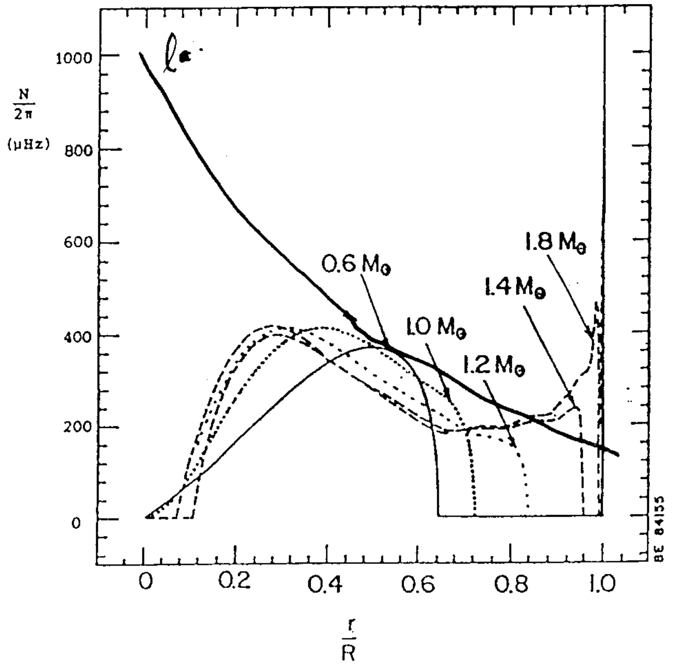

Figure 3. The buoyancy frequency N in ZAMS models, against fractional radius r/R. The masses of the models (in solar units) are indicated (from Christensen-Dalsgaard 1984a).

Table II. Precise Doppler techniques

Lines	Spectrometer	Reference	$\lambda/\Delta\lambda$	Noise $(m/s)^2$ Hz^{-1}	Literature
1	Fabry-Perot	none	110000	10000	Traub *et al.* (1978)
1	Fabry-Perot	capacitance	~12000	54000	Pietraszewski *et al.* (1986)
1	Fabry-Perot	capacitance	50000	(>10)	Butcher & Hicks (1986)
1	Michelson	atomic emission line	~10000	3000000	Pietraszewski *et al.* (1986)
1	K vapor filter	none	?	180000	Isaac & Jones (1986)
2	Na vapor filter	none	50000	10000	Fossat *et al.* (1982)
2	Na vapor filter	none	?	?	Rhodes *et al.* (1986)
~10	coudé	atm O_2	63000	13000	Smith (1983)
~10	coudé	HF abs cell	61000	27000	Campbell (1983)
~100	FTS	N_2O abs cell	85000	1000000	Hall & Hinkle (1981)
~300	echelle	Fabry-Perot	90000	300000	McMillan *et al.* (1985)
~1000	coudé	Fabry-Perot	50000	(~100)	Cochran & Young (1985)
>1000	echelle	Fabry-Perot + stable laser	?	?	Connes (1985b)
		Fabry-Perot			Ando (1986)

Table III. Precise Photometric techniques

Spatial channels	λ channels	$\lambda/\Delta\lambda$	Noise $(\Delta I/I)^2$ Hz^{-1}	Detector	Literature
1	1	~4	3×10^{-4}	pmt	Kurtz (1984)
1	1	400	2×10^{-4}	pmt	Duvall & Harvey (1983)
1	1	10	3×10^{-4}	pmt	Deubner & Isserstedt (1983)
1	2	40	1×10^{-6}	pmt	Duvall & Harvey (1985)
1	2	4000	6×10^{-3}	pmt	Noyes *et al.* (1984)
1	2	400-4000	?	pmt	Nisenson *et al.* (1986)
1	2	50000	?	Si diode	Butcher & Hicks (1986)
1	many	~30000	?	ccd	Brown *et al.* (1986)
3	1	~30	?	Si diode	Borucki (1984)
many	1	~4	5×10^{-4}	ccd	Walker (1984)
many	1	~4	2×10^{-3}	ccd	Howell & Jacoby (1986)
many	1		?	ccd	McGraw *et al.* (1986)

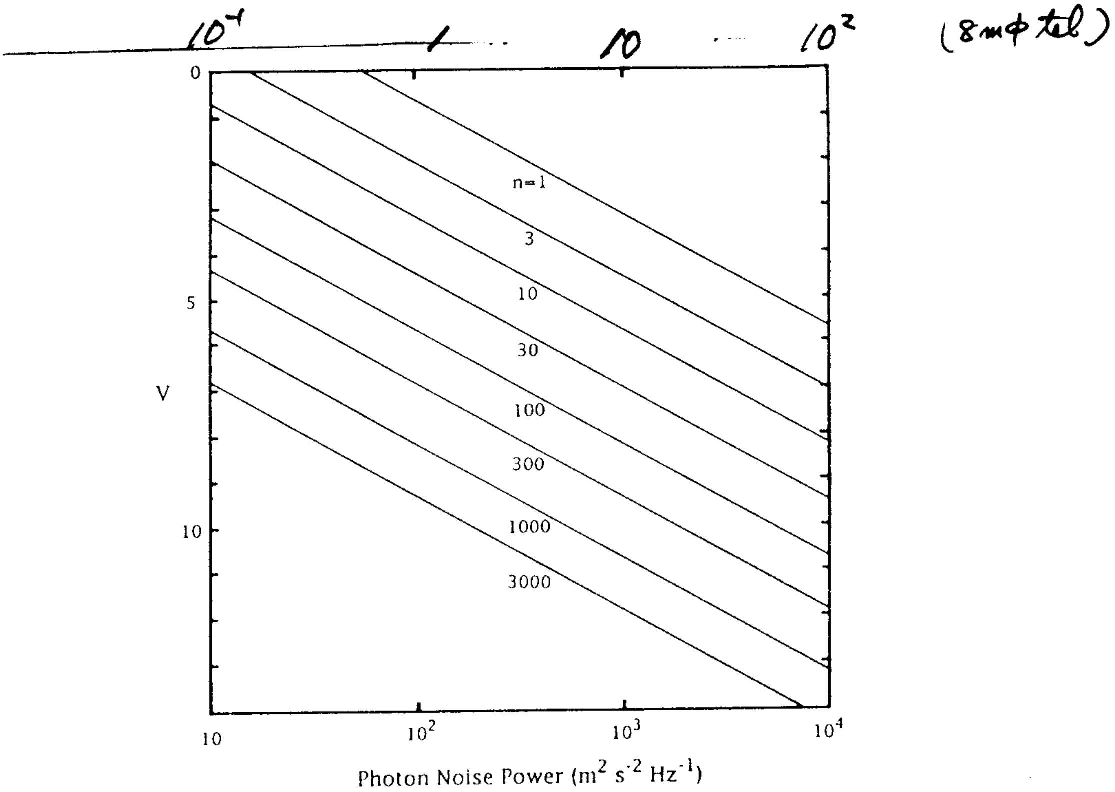

Figure 1. Visual magnitude *vs.* noise power density for a Doppler shift measurement due to photon noise as a function of the number, *n*, of spectrum lines observed simultaneously with a 100% efficient 1-m telescope. The spectrum lines are assumed to have a full width at half maximum of 8 km/s and the wavelength is 5500Å.

$$P = W_{line} / (150\, n d^2\, 10^{-0.4V})$$

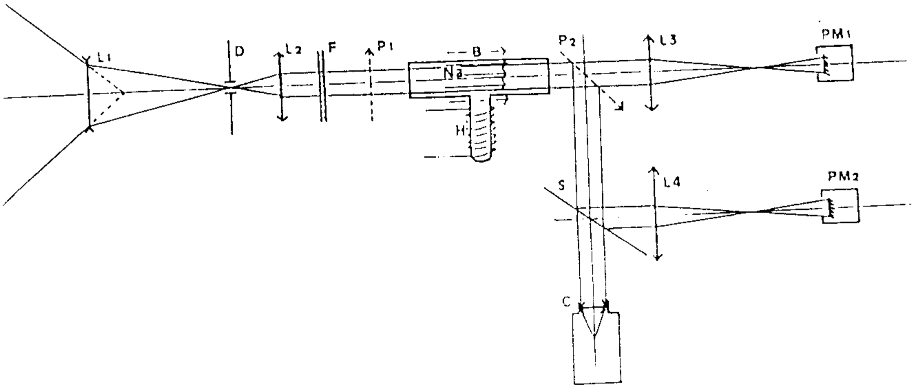
L1
D
L2
F
P1
B
Na
H
P2
L3
PM1
S
L4
PM2
C

Fig 2. Optical scheme of the instrument. The beam passes through a Barlow lens L1, the diaphragm D, the second lens L2, the interferential filter F, the polarizer P1 before the sodium-cell which is heated and is inserted in a magnetic field. At the output, it is split in two different polarizations by the Foster prism P2. The two beams then feed the photomultipliers PM1 and PM2. C is a guiding T.V. camera.

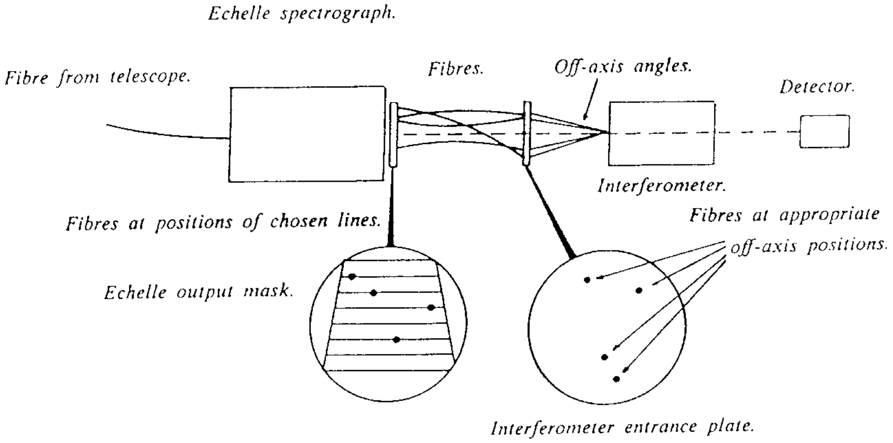
Echelle spectrograph.
Fibre from telescope.
Fibres.
Off-axis angles.
Detector.
Interferometer.
Fibres at positions of chosen lines.
Fibres at appropriate off-axis positions.
Echelle output mask.
Interferometer entrance plate.

Figure 1. Multi-lining a general MISOS instrument with 4 fibres.

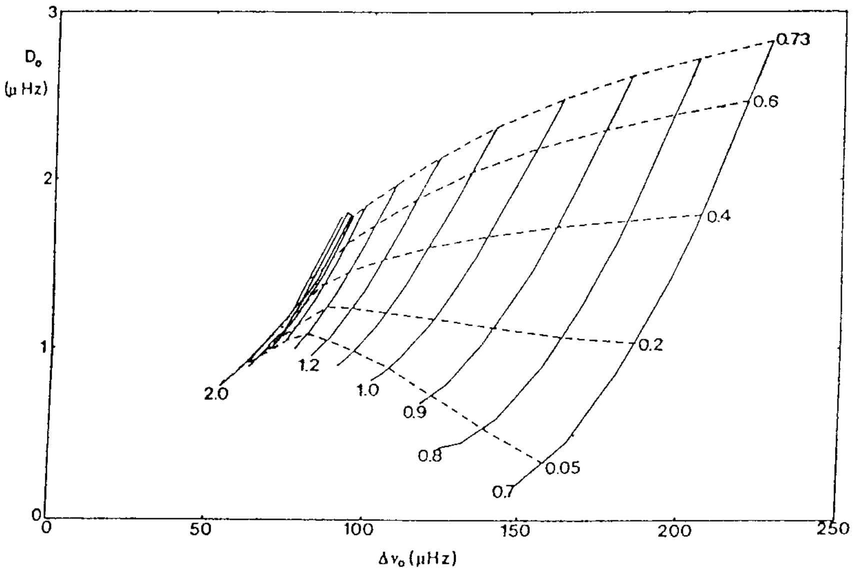

Figure 1. Evolution tracks ———————— and isopleths, - - - - - - - - - - in an "oscillation HR-diagram". The masses, in solar units, and the values of the central hydrogen abundance for the isopleths, are indicated.

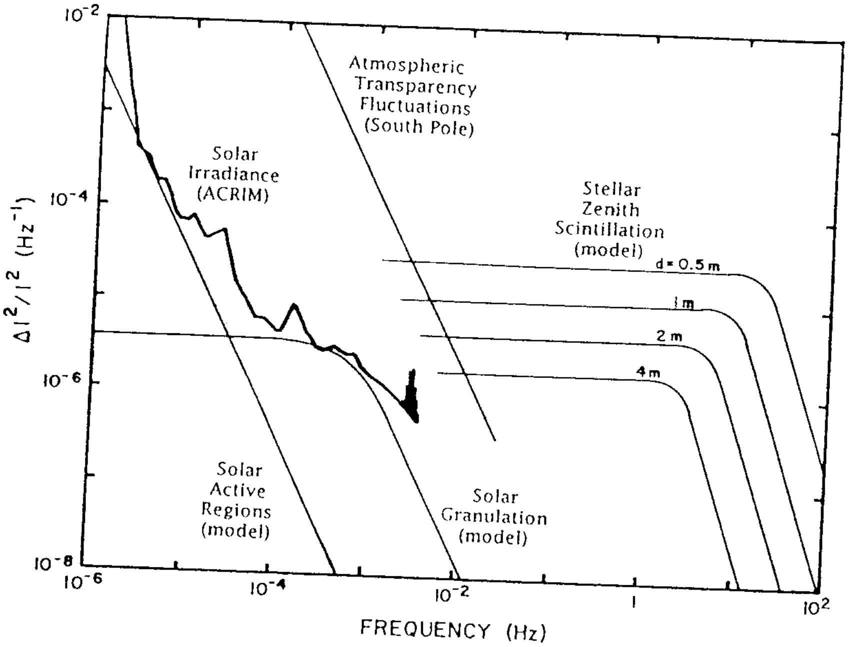

Figure 3. Noise power density spectrum of photometric measurements. Measurements of the sun are shown from the ACRIM Instrument (Woodard, 1984) along with a crude model attributing the solar spectrum to active regions and granulation. Atmospheric transparency noise measurements were made at the South Pole by Duvall, Harvey and Pomerantz. Scintillation noise is shown for telescopes of different diameters observing at the zenith, a wind velocity of 30 m/s and a ground altitude of 2 km.

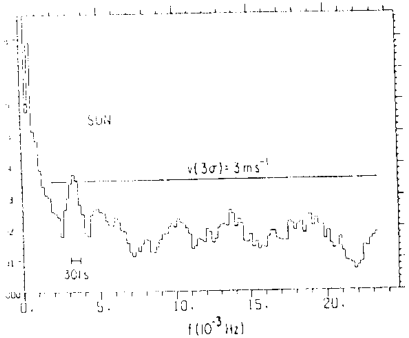

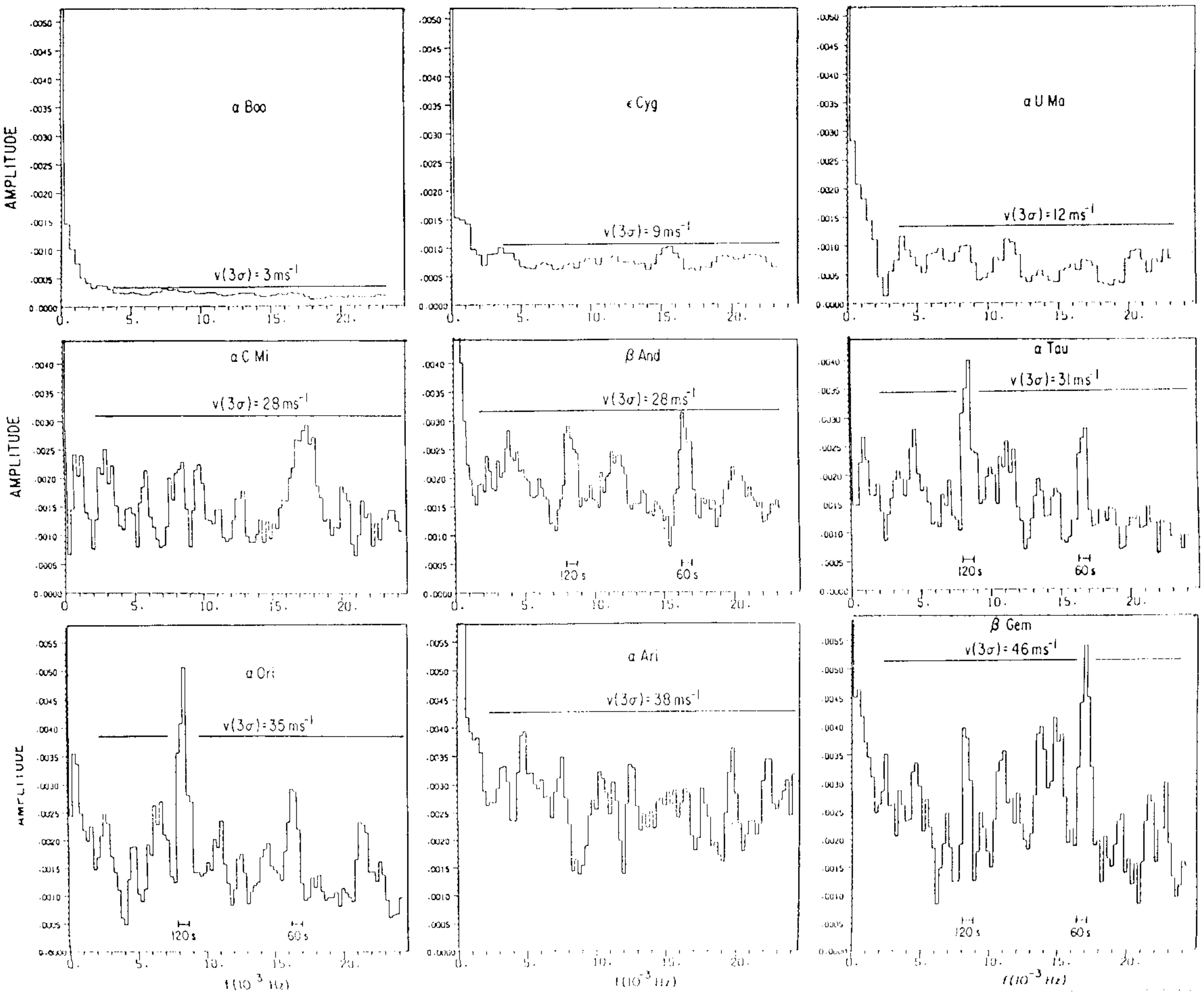

1.—The frequency-domain amplitudes as calculated the Fourier transform of the time-domain intensity in ng of the Fe line at 6678 Å for the integrated solar disk. requency data have been smoothed by a running 5-point ge—i.e., over about 1.0 mHz—as indicated by a short The local peak near 3.3 mHz corresponds to the well- n 300 s solar oscillation. The long horizontal line indi- a 3 σ level, below which features are not considered to be icant.

α CMi
(Procyon)

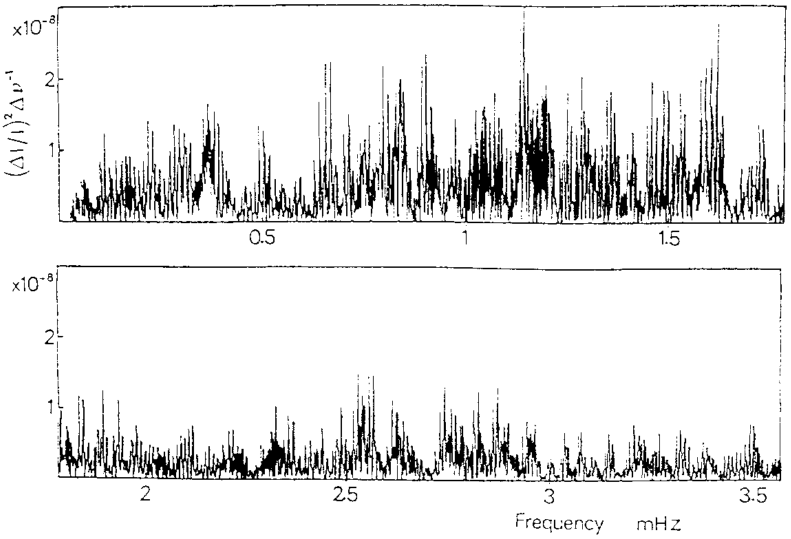

Fig. 4. Power spectrum of the four nights
monochromatic photometric signal record
Procyon, and taken as one single time seri
The frequency bin is $\Delta\nu = 1.74\,\mu$Hz and th
resolution of the data is $3.5\,\mu$Hz

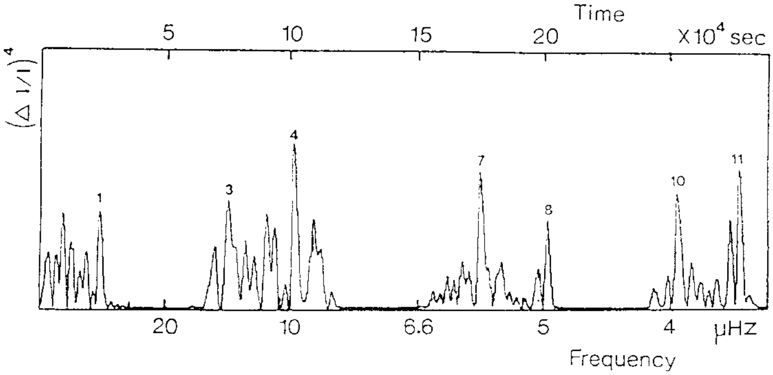

Fig. 5. Power spectrum of the 1.17–1.65 mH
range of Fig. 4. The autocorrelation of the
window function is clearly visible, as well as
regular pattern of equidistant peaks, in whic
Nos. 1, 3, 4, 7, 8, 10, 11 are permitted by thi
window function. The period of the fundame
(about 2.5 10^4 s) is the beating period betwee
consecutive harmonics of like degree. This pe
defines the spacing $\Delta\nu/2 = 39.7\,\mu$Hz

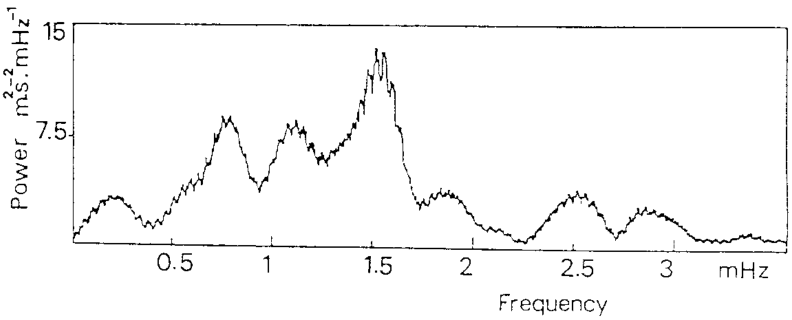

Fig. 6. By Fourier transform of the full Fi
by selection in this transform of the seven
bandwidths defined by the harmonics of Fi
and by inverse Fourier transform, a filtere
power spectrum is obtained, and this is its
envelope, shown at a resolution of 0.08 mH
The P-modes frequency range of Procyon
appears to be 0.6–1.7 mHz

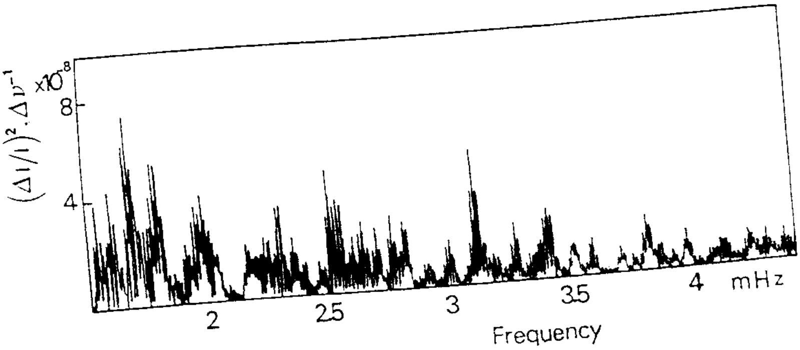

Fig. 9. Power spectrum of the 3
24 May 1983) or recording on
showing the range of interest fo
oscillation. Looking carfully to
(3–4 mHz) of this figure, one c
discriminate visually the regula
limit of the noise level. The fre
2.044 μHz, while the resolution
5.3 μHz

α Cen

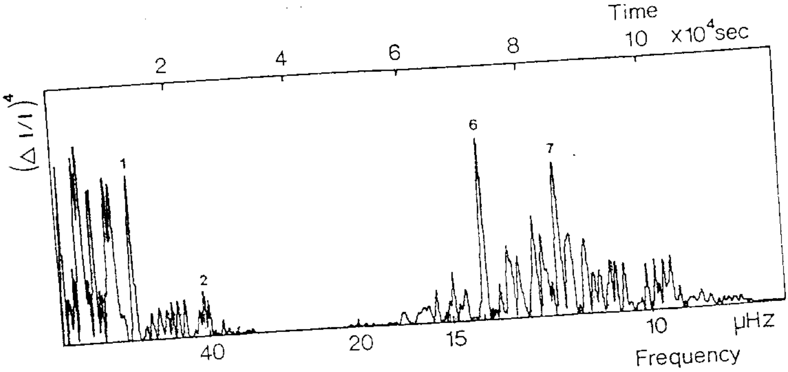

Fig. 10. Power spectrum of the 2.3
range of the previous figure. Only t
the window function are shown. Th
at (81.3 μHz)$^{-1}$ is present and labe
Peaks No. 2, 6, and 7 are also visib
to a more precisely defined value o
for $\Delta\nu/2$. The very short third nigh
show any other harmonic

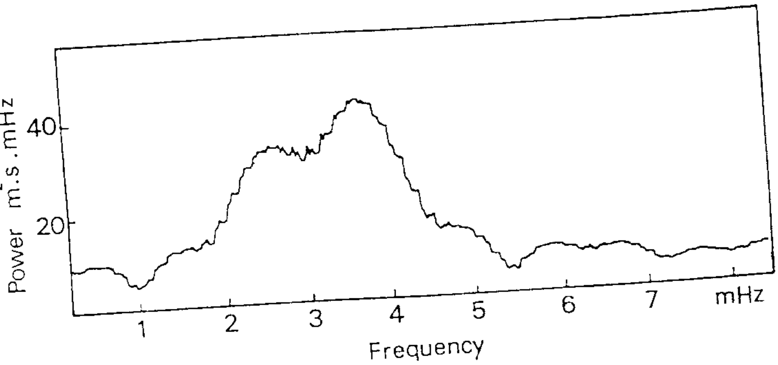

Fig. 11. By Fourier transform of
by selection in this transform of
bandwidths defined by the Fig. 1
Fourier transform, a filtered po
obtained and this is its envelope
resolution of 0.04 mHz. The *p*-m
range (2–5 mHz) is confirmed t
the solar one

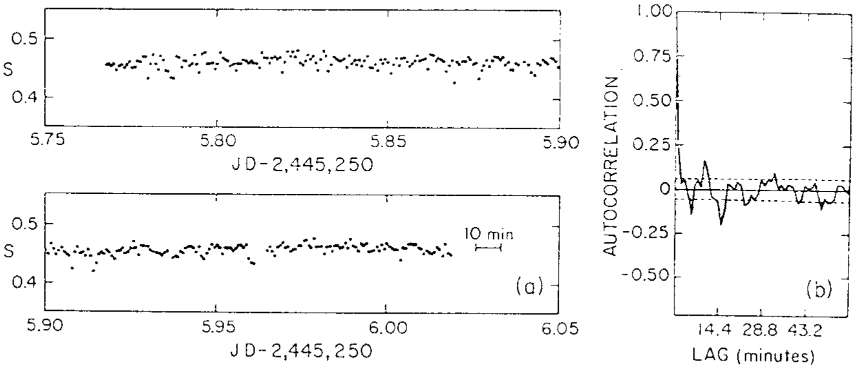

FIG. 1.—(*a*) Sky-corrected HK flux index *S*, observed at 67 s intervals for 6 hr on 1982 October 13. (*b*) Autocorrelation function of the data set 1*a*; the dashed lines give 1 σ error estimates for the peaks in the autocorrelation function (see Baliunas *et al.* 1983).

ε Eri

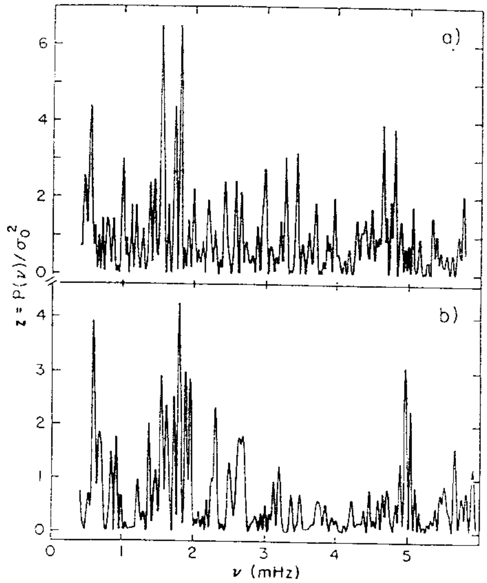

FIG. 2.—(*a*) Power spectrum of the data of 1982 October 13 1*a*). (*b*) Power spectrum from the data of 1983 November 29. In spectra power is plotted in units of the variance σ^2 of the data, list Table 1.

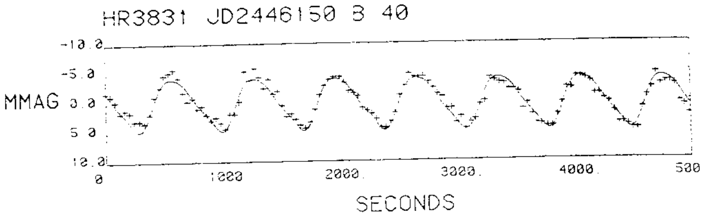

Figure 3 A portion of the light curve of HR 3831 near pulsation maximum (40-s int
grations). Note the obvious nonlinear shape of the light curve.

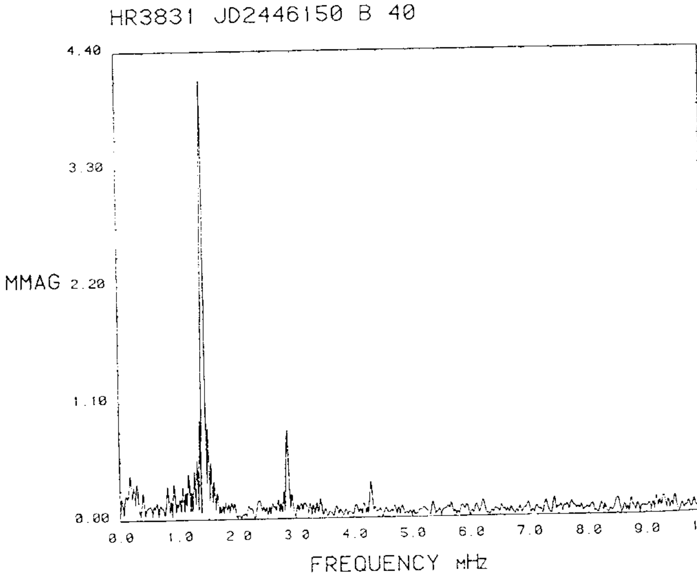

Figure 4 The amplitude spectrum of the entire 5.8-hr light curve obtained on JD 2446
(a portion of which is shown in Figure 3). The principal frequency and its first two harmo
are clear; there are no other significant frequencies. Note that at higher frequencies, w
the noise is scintillation limited, the highest noise peaks are less than 0.2 mmag for this si
light curve obtained with the *SAAO* 0.75-m telescope.

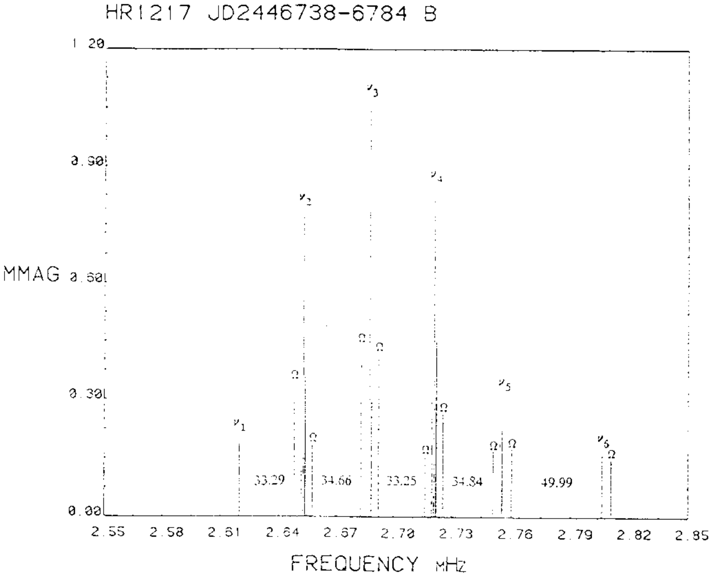

Figure 10 A schematic amplitude spectrum for HR 1217, showing its striking similarity to the solar low-*l* *p*-mode amplitude spectrum. The spacing of the principal frequencies is to scale; the separations are in microhertz. The rotational sidelobes are marked Ω; their separations and the separations of the secondary frequencies from the principal frequencies have been exaggerated for clarity (from 104).

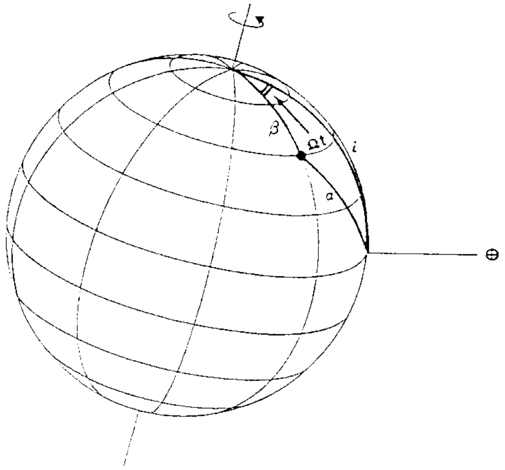

Figure 1 The geometry of an oblique rotator. The rotational inclination is i, the magnetic obliquity is β, and the rotation frequency is $\Omega = 2\pi\nu_{rot}$, where phase zero is taken to be at magnetic maximum.

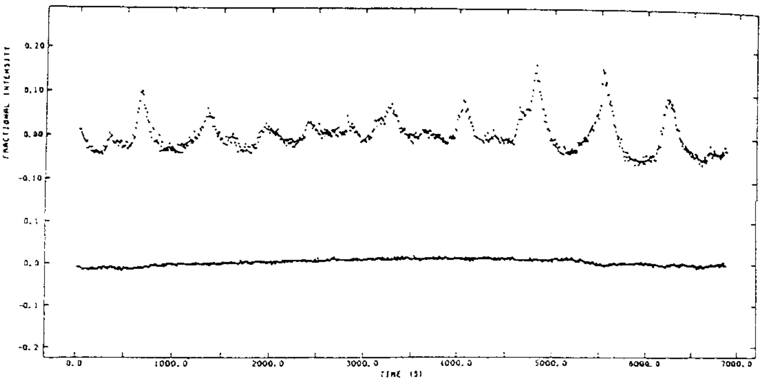

Figure 2. Light curve of the DBV GD 358 and comparison star, obtained with a two-star pl tometer under photometric conditions (compare with bottom panels in Fig. 1).

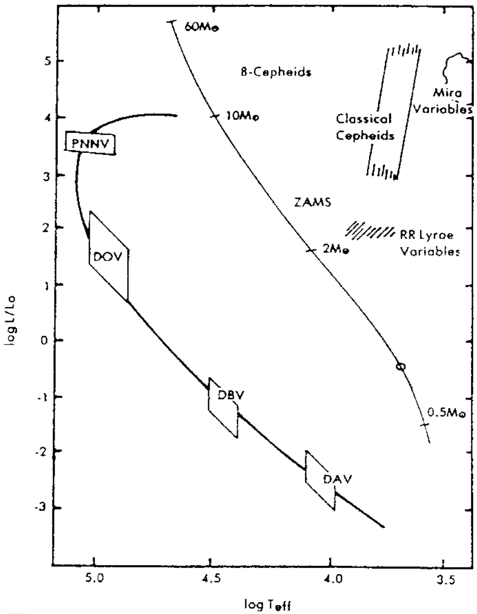

Figure 3. The compact pulsators in the H-R diagram.

has more than 25 (GD 358, Winget *et al.* 1982b). The beating together of these oscil results in occasionally very high and very low amplitudes in the light curves.

The spectroscopic information is particularly revealing for the two cooler clas compact pulsators. The DBV stars have only surface helium present in their sp and the only thing which sets them apart from the nonvariable DB stars is that th found only near the He I opacity maximum. By the same token the DAV stars hav surface hydrogen present, and are found only near the very well defined opacity ma

TABLE 1

Period Changes in Compact Pulsators

Name	Class	Π (s)	$\lvert\Pi/\dot{\Pi}\rvert_{obs}$ (yr)	$\lvert\Pi/\dot{\Pi}\rvert_{theor}$ (yr)	Ref.
PG1159–035	DOV	516	$(1.4 \pm 0.1) \times 10^6$	$\sim 10^6$	1
PG1351+489	DBV	489	$> 3 \times 10^5$	$\sim 3 \times 10^5$	2
G117–B15A	DAV	215	$> 6.9 \times 10^8$	$\sim 4 \times 10^9$	3
R548	DAV	213	$> 3 \times 10^7$	$\sim 4 \times 10^9$	4
L19–2	DAV	114	$> 9 \times 10^6$	$\sim 4 \times 10^9$	5

1. Winget *et al.* (1985); 2. J. A. Hill (1986, private communication); 3. Kepler *et al.* (1987); 4. Stover *et al.* (1980); 5. O'Donoghue *et al.* (1982).

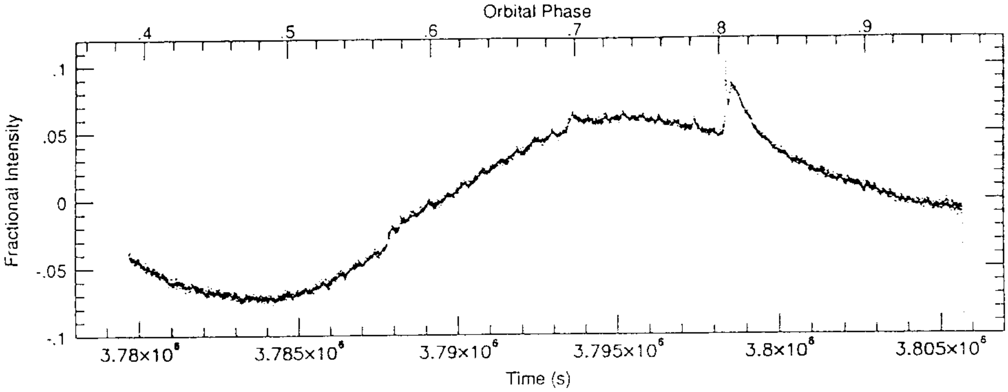

FIG. 1.—*U*-band light curve of V471 Tau acquired with the 3.6 m CFHT

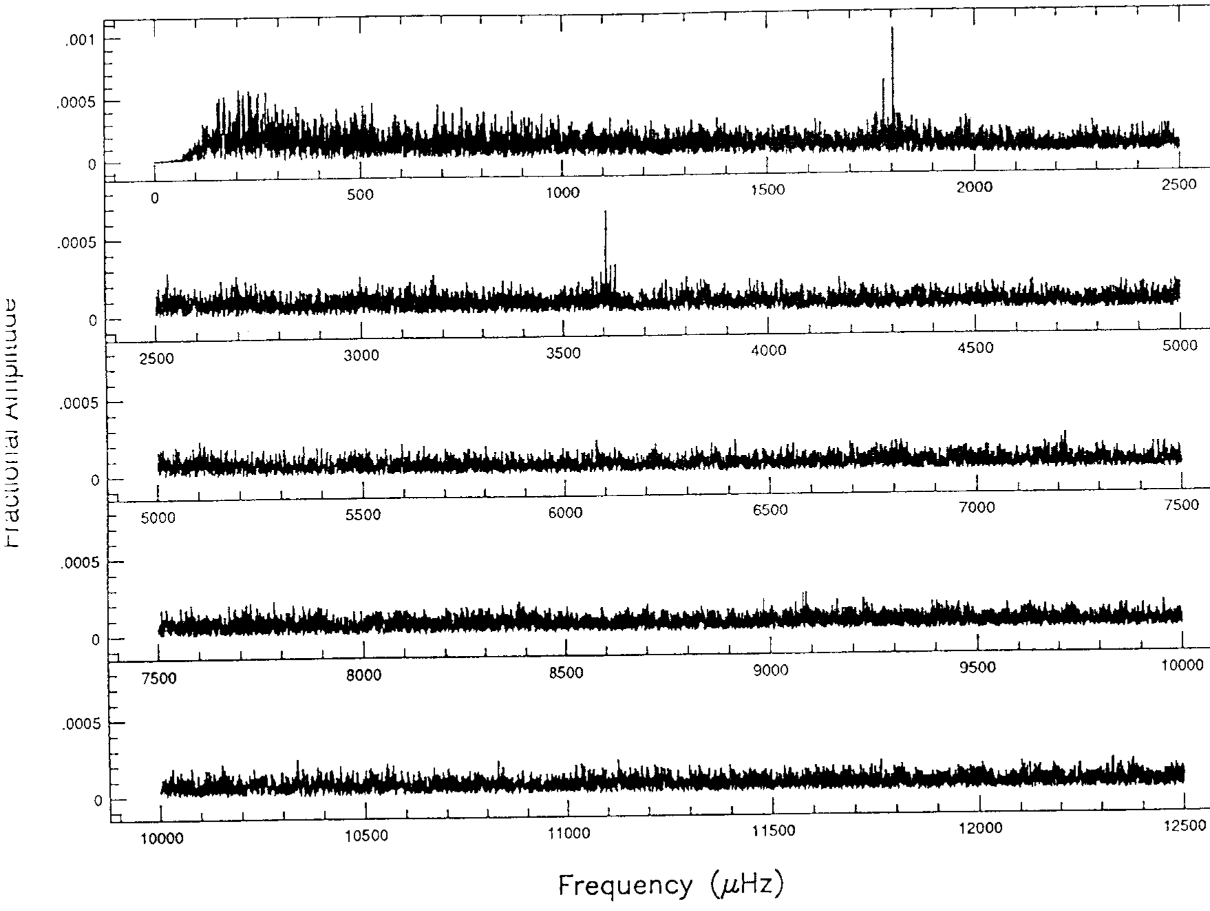

FIG. 2.—Amplitude spectrum of the V471 Tau WET data

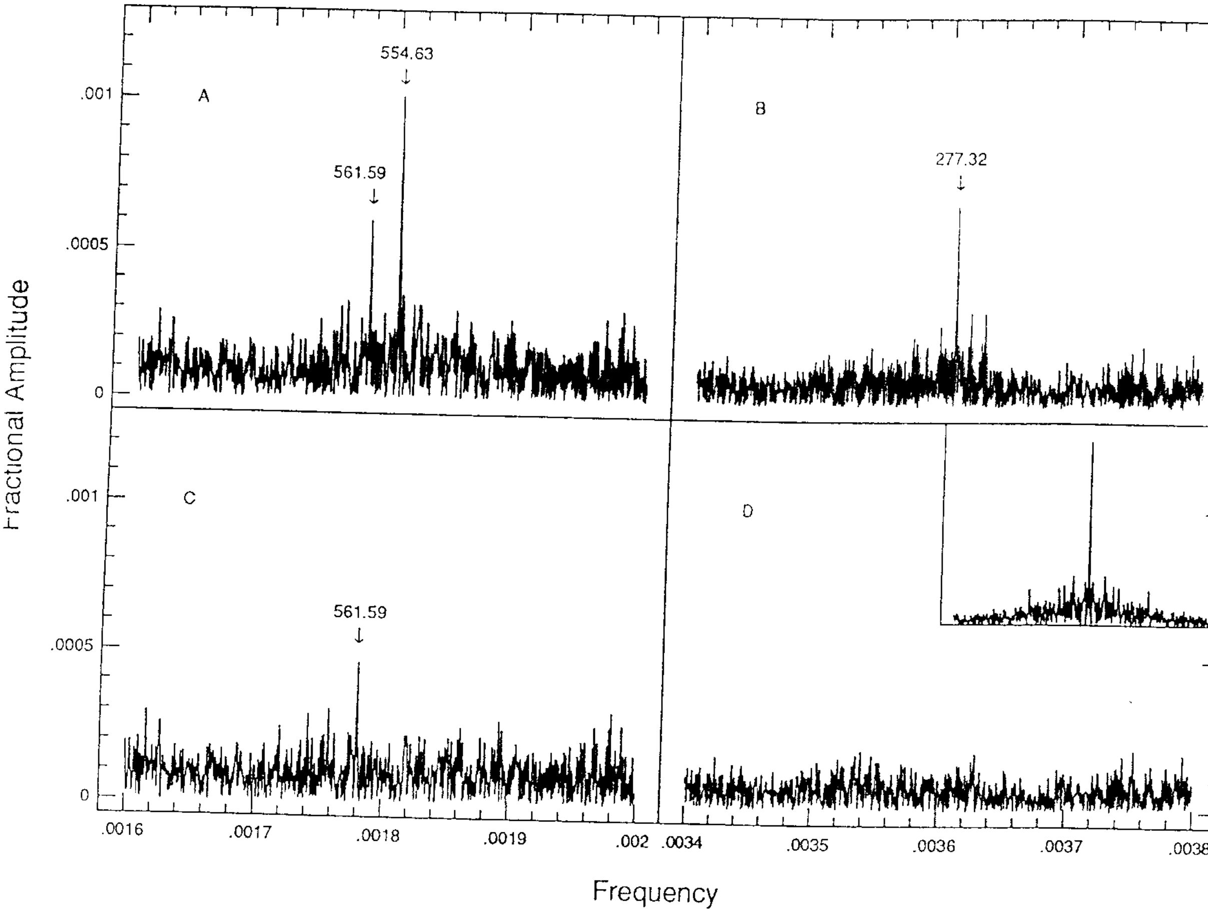

FIG. 3.—Enlarged amplitude spectra of V471 Tau WET data. Fig. 3c and Fig. 3d show the residuals after the periodicities at 555 s and 277 s have been removed. The inset shows the spectral window.

where r, θ, and ϕ refer to the radial, polar, and azimuthal directions, respectively, P_l^m is the associated Legendre function, V_p is the pulsation amplitude, and k an assumed constant of proportionality between the horizontal and vertical motions.

We assumed that the modes were prograde sectorial modes ($l = -m$), although a number of trials with other modes were made. Theory and observations suggest that these modes are the most likely to be excited, and they produce the largest possible line profile variations while minimizing the radial velocity variation. For these modes, the value of l determines the degree of concentration of the oscillations toward the stellar equator (the pulsation velocity is proportional to the cosine of the latitude to the lth power), while the value of $|m|$ describes the number of wave crests along the equator. The sign of m simply describes the direction in which the running waves are moving; positive values apply to waves moving opposite to the direction of stellar rotation, while negative values apply to waves moving in the same direction as the star's rotation.

c) Results

Figure 15 shows theoretical line profiles of the He I λ6678 line for models with (l, $-m$) ranging from 1 to 10. The pulsation amplitude was chosen to be 20 km s^{-1}, the k value is 0, the projected rotation velocity is 370 km s^{-1}, and all of the models are computed at the same phase. It is obvious that all of the modes with l values greater than unity are readily visible, in contradiction to the expectation of previous researchers. In fact, the visibility of the modes actually increases with increasing order. This unexpected result is a consequence of the very rapid rotation of the star, which allows us to resolve the velocity structure across the disk of the star in a manner analagous to that discussed in § IV.

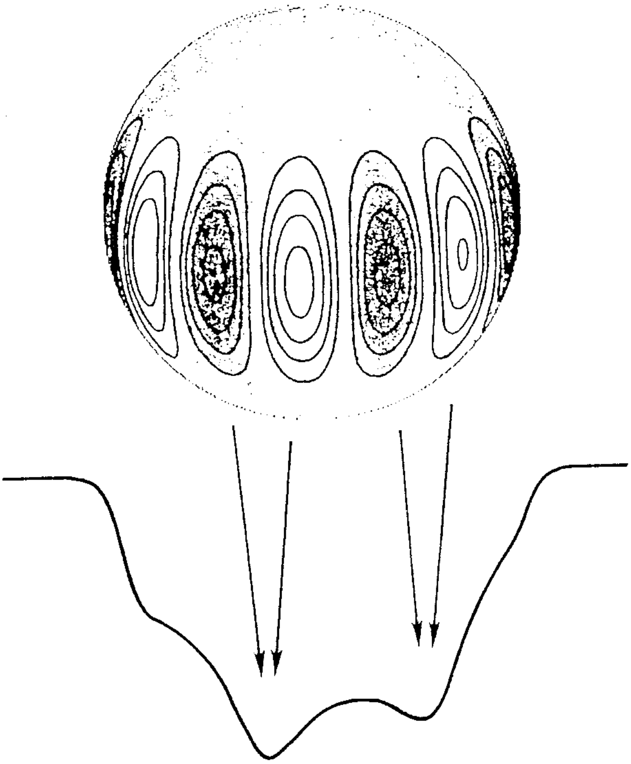

FIG. 16.—Illustration of the formation of distortions in the line profiles of a rapidly rotating nonradially oscillating star. This is a velocity map of the star with the resultant line profile shown below. The width of the line profile has been scaled to match the diameter of the star, thus reflecting the mapping which occurs between position across the disk and position across the line profile. The darkest shaded regions correspond to material moving away from the observer, while the lightest regions represent material moving toward the observer. Contours are drawn every 5 km s^{-1}.

simultaneous broad-band photometry, while the nonradial oscillation model seems capable of reproducing many of the observed peculiarities of the star. We will then propose a theoretical model which explains the occasional Be type outbursts of this star, and the Be star class in general, in the context of these nonradial oscillations.

II. THE OBSERVATIONS

All of our spectral observations were obtained with the unintensified Reticon system and coudé spectrograph of the Lick Observatory Shane 3 m telescope and Coudé Auxiliary Telescope (CAT). A complete description of the Reticon system was presented elsewhere (Vogt 1981). The detectors were 2×936 and 1×1872 channel unintensified silicon photodiode arrays manufactured by Reticon Corporation, Sunnyvale, California. The arrays were operated at $-185°$ C in an evacuated LN$_2$ Dewar, at the focus of the 40 inch (1 m) camera of the coudé spectrograph. The observations were centered at λ6678, providing 140 Å of spectrum at either 0.075 Å/diode or 0.15 Å/diode with the 1×1872 and 2×936 arrays, respectively. The entrance slit of the spectrograph was set to project down to 2–4 pixels (8 pixels on the CAT) for an effective resolution of 150–300 mÅ or 6–13 km s^{-1}. Each individual observation generally achieved a signal-to-noise (S/N) ratio in excess of 600

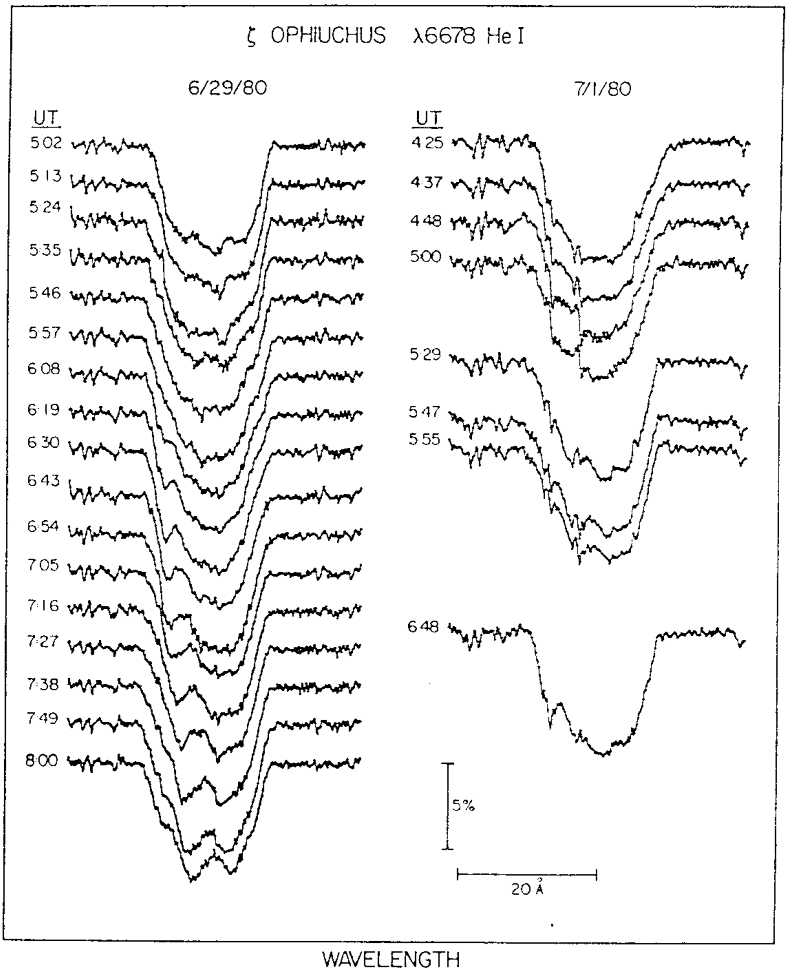

FIG. 1.—Observations of the He I λ6678 line of ζ Oph on 1980 June 29 and 1980 July 1 UT

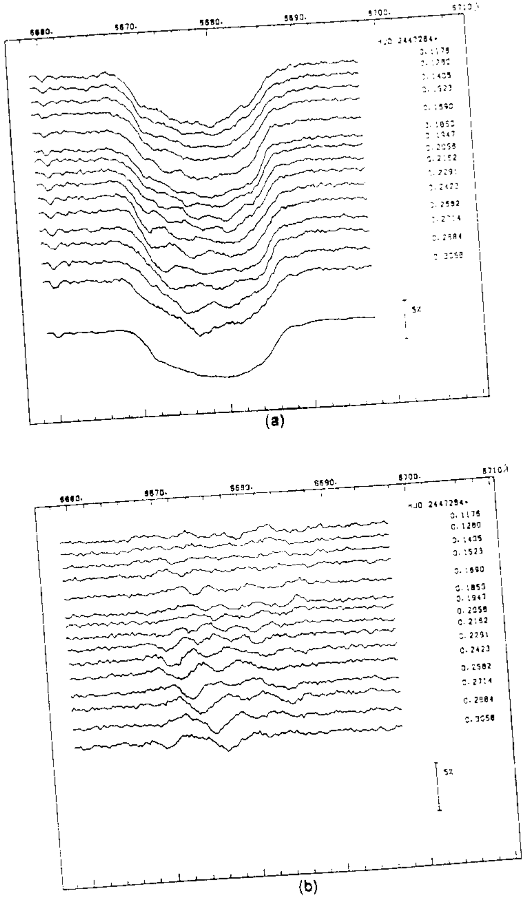

Fig. 6a and 6b. See the caption on page 705

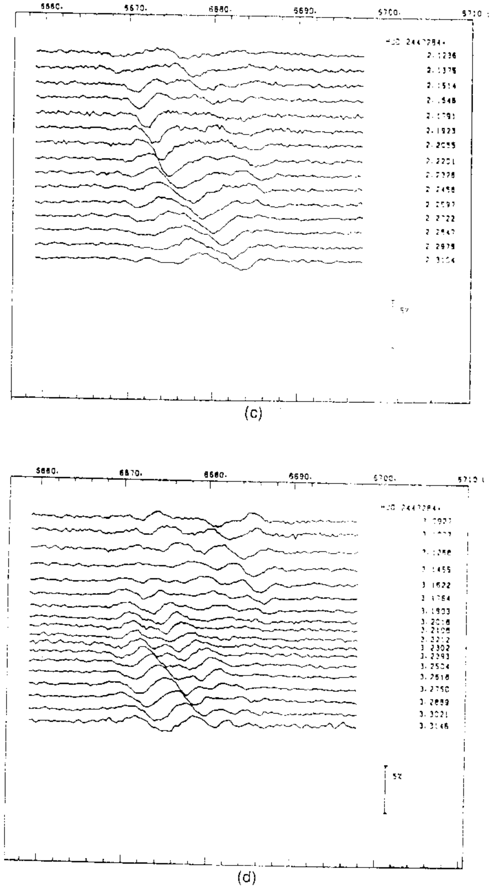

Fig. 6. The same as figure 5 but in 1988 May 2 to 5. Forty-eight profiles ((a) or (b) to (d)) were obtained in this season.

Table 7d. Estimated (m, period) in wavelength domain.

Candidates for m	Estimated periods (hr)
-4 ± 1	3.32 ± 0.3
-7 ± 1	2.44 ± 0.2
-9 ± 1	2.00 ± 0.3

Table 7e. Identified modes in 1988 May.

m	Period (hr)	k	$\|\|mP\|\|$
-4 ± 1	3.33 ± 0.1	0.2 ± 0.1	10 - 16
-7 ± 1	2.44 ± 0.08	0.2 ± 0.1	15 - 20
-9 ± 1	1.86 ± 0.05	0.2 ± 0.1	15 - 18

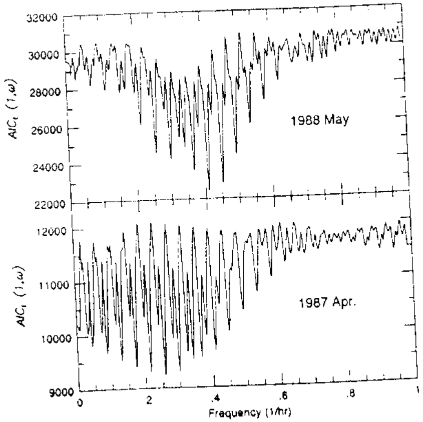

Fig. 7. Values of $AIC_t(1,\omega)$ in the temporal domain for both seasons. Aliasings are conspicuous, though more than one independent peaks are visible in both seasons.

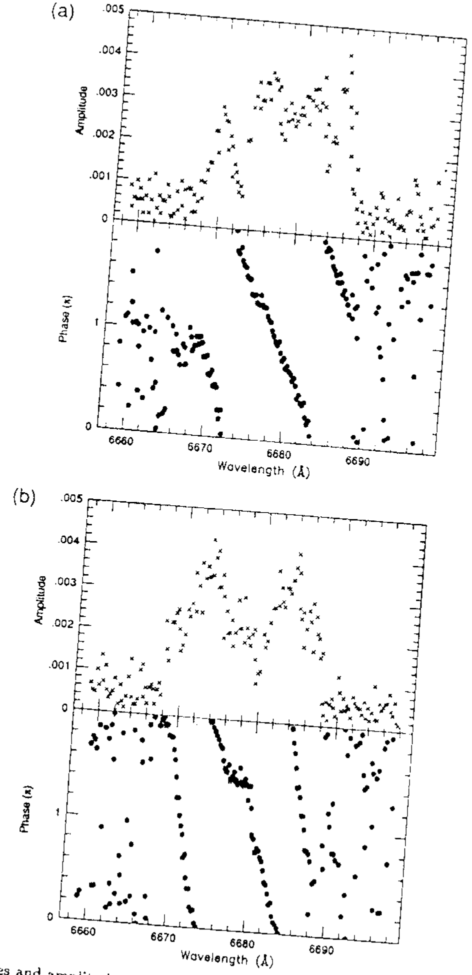

Fig. 8. Phases and amplitudes for the first two sinusoidal waves selected in temporal domain for 1987 April data. The phases of the waves with periods of 3.89 hr (a) and 2.72 hr (b) change systematically with time.

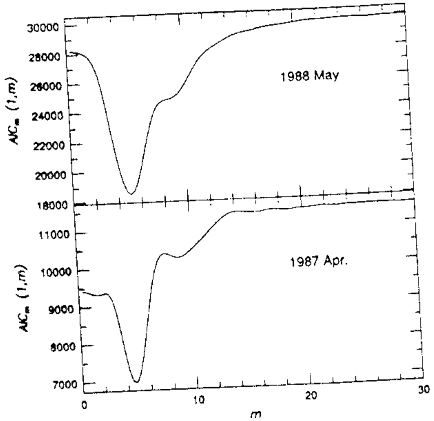

Fig. 10. $AIC_m(1, m)$ values in the wavelength domain for both seasons. At least two peaks can be seen at almost the same positions ($m \sim 5$ and $m \sim 9$) for both seasons.

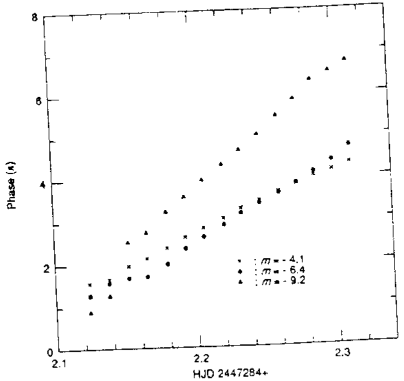

Fig. 11. Phases of the selected three sinusoidal waves in the wavelength domain for the data of 1988 May. The phases of these waves change stably and systematically so that the periods of NRP can be derived from these phase speeds.

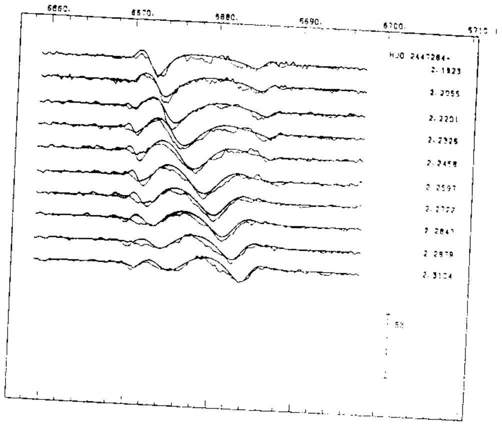

Fig. 12. Comparison of the observed profiles (last ten profiles obtained in 1988 May 4) with the theoretically calculated ones. Only the absolute amplitude of NRP is a free parameter in this fitting and the other parameters can be specified in our mode analysis.

mode with a period of 2.44 hr seems to slightly change (see section 4). **Assuming** that $l = -m$, the amplitudes of the oscillations can be determined by the line profile fitting method. In figure 12, the expected line profile variation and the observed one are compared for the data of May 4 in 1988. Here, the equatorial velocity of the star V_e is 400 km $s^{-1}$and the inclination, i, is 90°. We can see in this figure that the bump features are well reproduced by these modes. The relative amplitudes of the modes in the simulation are $A_4/A_7 = 0.9$ and $A_9/A_7 = 0.65$ and the maximum velocity amplitude of oscillations is about 24 km s^{-1}. These evaluated amplitudes might be larger than the actual amplitudes of oscillations, because the calculated intrinsic profile is much weaker than the observed one. In fact, we require an accurate estimation of the shape and the strength of the intrinsic profile and the extent of the gravity darkening to evaluate the amplitudes of the oscillations correctly. Thus, we use the amplitudes of fitted sinusoidal waves itself to examining the long-term variability of the oscillations.

4. Discussion and Summary

4.1. Limits of Our Method of Mode Identification

The period and the modal order analyses are found to be useful for identifying sectoral NRP in rapidly rotating stars. However, there are some